



OPEN ACCESS

EDITED BY

Saadat Majeed,
Bahauddin Zakariya University, Pakistan

REVIEWED BY

Chunyan Li,
Jilin University, China
Manlin Qi,
Jilin University, China

*CORRESPONDENCE

Jie Liu,
✉ 18661801995@163.com
Xue Li,
✉ lixue@qdu.edu.cn

†These authors have contributed equally to this work.

RECEIVED 02 February 2024

ACCEPTED 22 March 2024

PUBLISHED 11 April 2024

CITATION

Hou W, Lin Z, Xia X, Sun S, Niu Z, Liu J, Lu J, Yin D and Li X (2024), Antibacterial and anti-inflammatory polyethyleneimine/polyacrylic acid hydrogel loaded with CeO₂ quantum dots for wet tissue wound dressings. *Front. Mater.* 11:1379836. doi: 10.3389/fmats.2024.1379836

COPYRIGHT

© 2024 Hou, Lin, Xia, Sun, Niu, Liu, Lu, Yin and Li. This is an open-access article distributed under the terms of the [Creative Commons Attribution License \(CC BY\)](https://creativecommons.org/licenses/by/4.0/). The use, distribution or reproduction in other forums is permitted, provided the original author(s) and the copyright owner(s) are credited and that the original publication in this journal is cited, in accordance with accepted academic practice. No use, distribution or reproduction is permitted which does not comply with these terms.

Antibacterial and anti-inflammatory polyethyleneimine/polyacrylic acid hydrogel loaded with CeO₂ quantum dots for wet tissue wound dressings

Wenxue Hou^{1,2†}, Zehui Lin^{3†}, Xiaomin Xia^{1,2}, Sa Sun^{1,2}, Zhaojun Niu^{1,2}, Jie Liu^{1,2*}, Jiqing Lu⁴, Dongming Yin⁵ and Xue Li^{1,2*}

¹Department of Stomatology, The Affiliated Hospital of Qingdao University, Qingdao, China, ²School of Stomatology, Qingdao University, Qingdao, China, ³Institute of Materials for Energy and Environment, College of Materials Science and Engineering, Qingdao University, Qingdao, China, ⁴Key Laboratory of the Ministry of Education for Advanced Catalysis Materials, Institute of Physical Chemistry, Zhejiang Normal University, Jinhua, China, ⁵State Key Laboratory of Rare Earth Resources Utilization, Changchun Institute of Applied Chemistry, Chinese Academy of Sciences, Changchun, China

Searching for an antibacterial and anti-inflammatory dressing that can stably adhere to wet tissues remains a momentous clinical challenge, especially in the context of treatment failure due to multi-drug-resistant bacteria. Using a hard template method in combination with an *in situ* chelating strategy, three-dimensional nitrogen-doped graded porous carbon anchored 1.5–2.5 nm CeO₂ quantum dots (CeO₂-QDs) were tailor-designed in this study. Using the size effect, CeO₂-QDs have a higher percentage of Ce³⁺ and oxygen vacancies that could amplify their antibacterial effects. Polyethyleneimine/polyacrylic acid (PEA) powder could self-gel and be adhesive due to its strong physical interactions, which make it an ideal carrier for CeO₂-QDs. PEA@50 (mg/mL) CeO₂-QDs hydrogel and PEA@75 (mg/mL) CeO₂-QDs hydrogel with moderate doses of CeO₂-QDs show a superior antibacterial effect against *Staphylococcus aureus* (*S. aureus*) and *Escherichia coli* (*E. coli*) strains. Furthermore, PEA@50CeO₂-QDs hydrogels possess excellent anti-inflammatory capacity through their antioxidant activity, which could promote macrophage M2 phenotype polarization. More importantly, cytotoxicity assays on L929 fibroblasts show that PEA@CeO₂-QDs hydrogels have no significant toxicity, and a significant proliferative effect could be observed. Overall, PEA@50CeO₂-QDs hydrogels have the potential to become a multifunctional wet tissue dressing with anti-inflammatory and antiseptic properties to promote the healing of infected wounds.

KEYWORDS

CeO₂ quantum dots, polyethyleneimine/polyacrylic acid hydrogel, antioxidation, antimicrobial, anti-inflammatory

1 Introduction

According to recent research, the global wound care market was valued at USD 18.4 billion in 2018 and was anticipated to grow constantly at an annual growth rate of 3.9% from 2019 to 2026 (Monika et al., 2021). Among various types of wounds, wet tissue damage, such as mucosal wounds resulting from surgical incisions, traumatic injuries, or persistent ulcers, is prone to cause infection and prolonged inflammation. The incidence of postoperative infection in patients with oral or oropharyngeal cancer has been reported to be approximately 59% (Belusic-Gobic et al., 2020). With the recognition of pathogens by resident immune cells and the aggregation of granulocytes and mononuclear phagocytes, the release of pro-inflammatory cytokines and removal of cellular debris and microorganisms could be initiated through mechanisms such as the production of reactive oxygen species (ROS) (Kolaczowska and Kubes, 2013; Feehan and Gilroy, 2019). Furthermore, the overuse of antibiotics in clinical settings has led to the emergence of antibiotic-resistant microbial strains. In addition, due to the transient and erratic antibacterial effect of antibiotics caused by saliva secretions or other body fluids, the therapeutic effect of antibiotics or other antibacterial agents on infection is limited in reality (Guan et al., 2022). Given all of the above observations, it is imperative to present a dressing capable of securely and tenaciously adhering to the mucosa to exert both antibacterial and anti-inflammatory functions.

Based on the transition between Ce^{3+} and Ce^{4+} , CeO_2 has antioxidant enzyme mimic activity and gained effective antibacterial, anti-inflammatory, and antioxidant properties. The interconversion of Ce^{3+} and Ce^{4+} in CeO_2 is in dynamic equilibrium and accompanied by the release or elimination of ROS (Schaube et al., 2019; Liu et al., 2022). The ROS produced by Ce^{3+} can disrupt the cell structure of bacteria and, hence, exhibit antimicrobial actions. However, the excess ROS in inflamed tissues could be removed by Ce^{4+} , which prevents further tissue damage. CeO_2 nanoparticles were frequently used in self-regenerating antioxidative and anti-inflammatory medicines for a variety of disorders based on their capacity to scavenge ROS (Kim et al., 2023; Meng et al., 2024; Yang et al., 2024). The tuning of particle size was reported to play an important role in determining the physical, chemical, and biological properties of CeO_2 (Hosseini and Mozafari, 2020; Luneau et al., 2023). Particularly, CeO_2 quantum dots (QDs) have drawn significant attention according to the size effect, which guaranteed enhanced surface exposure and profound structure modulation (Younis et al., 2013; Kong et al., 2018; Kar et al., 2022). CeO_2 QDs anchored to Ag/cellulose or La-doped CeO_2 QDs exhibit improved antibacterial ability (Ikram et al., 2021; Shahzadi et al., 2023). CeO_2 nanoparticles with smaller sizes of 5 or 10 nm were verified to significantly elevate antioxidant ability compared with nanoparticles of larger sizes (Kumar et al., 2018; Yang et al., 2019; Xia et al., 2022). It was validated that the ROS scavenging activity of CeO_2 QDs could be prominently improved by regulating the diameter to be approximately 2.8 nm. However, the applications of CeO_2 QDs in clinical treatment have been scarcely explored.

The presence of fluid secretion around moist tissues poses a challenge to the sustained efficacy of antimicrobial treatments in wound care. Thus, there is a demand to create antimicrobial drug carriers that securely attach to moist tissues. Polyethyleneimine/polyacrylic acid (PEA) hydrogel formed through the physical cross-linking of polyethyleneimine and polyacrylic acid has been extensively studied as potential biomaterials and gene delivery vehicles (Ji et al., 2019; Li et al., 2021). It possesses advantageous properties such as superior adhesion, elasticity, self-healing, biocompatibility, and *in situ* gel formation. These properties make it highly ideal in a variety of biomedical applications (Peng et al., 2021a; Fu et al., 2022; Wang et al., 2022). Peng et al. found that the PEA hydrogel could significantly promote the proliferation activity of the gastric mucosal epithelium and promote the healing of the gastric perforation mucosa due to which the angiogenesis of granulation tissue cells was more dynamic than that of suture and fibrin gel (Peng et al., 2021b). To summarize, the PEA hydrogel, with the potential to be applied as wet tissue dressings, is a predominant carrier with long-term pharmacological effects.

Herein, a hard template combined with an *in situ* chelating strategy was developed to deliver CeO_2 QDs confined by a 3D N-doped porous carbon (CN) scaffold, i.e., three-dimensional nitrogen-doped graded porous carbon anchored 1.5–2.5 nm CeO_2 QDs. PEA hydrogels, which can tightly adhere to wet tissues, play the role of carriers to achieve a steady and decelerated release of CeO_2 -QDs. Thus, PEA hydrogels and CeO_2 -QDs complement each other for the promotion of wound healing, leading to excellent antibacterial activity. With systematic characterizations, the structure–function relationship is established, which will be valuable for advancing the clinical application of CeO_2 -based functional materials.

2 Methods

2.1 Materials and reagents

All the chemicals were used without any additional purification. Polyethyleneimine (Mw, ca. 70,000) aqueous solution (50 wt%) was supplied by Macklin (China). Polyacrylic acid (Mw, ca. 240,000) aqueous solution (25 wt%) was obtained from J&K Scientific (China). The RNA-easy isolation reagent was provided by Vazyme Biotech Co., Ltd. (United States). The ABScript III RT Master Mix for qPCR with a gDNA removal Kit and 2X Universal SYBR Green Fast qPCR Mix Kit were both purchased from ABclonal Technology (United States). Kits for the detection of catalase (CAT) and total antioxidant volume (T-AOC) were obtained from Solarbio (Beijing, China). Kits for the detection of superoxide dismutase (SOD) were purchased from Elabscience (Beijing, China). In addition to raw fibroblasts (I929, ScienCell, San Diego, CA, United States), mouse monocyte–macrophage leukemia cells (RAW 264.7 cell line), *Escherichia coli* (*E. coli*) ATCC 25922, and *Staphylococcus aureus* (*S. aureus*) ATCC 29213 were acquired from the American Type Culture Collection (ATCC, Manassas, VA). The Cell Counting Kit-8 (CCK-8) and other biological kits were purchased from Dalian Meilun Biotechnology Co., Ltd.

2.2 Preparation and characterization of CeO₂-QDs, PEA hydrogel, and PEA@CeO₂-QDs hydrogel

2.2.1 Synthesis of CeO₂-QDs

Polymethyl methacrylate (PMMA) was first produced following the method reported by Luo et al. (2018). Specifically, 700 mL of deionized (DI) water was used to dissolve 0.18 g of potassium persulfate powder (K₂S₂O₈). Afterward, the solution was heated to 70°C, protected by N₂. A measure of 53.7 mL of methyl methacrylate was added dropwise under continuous stirring at 70°C for 60 min. The suspension was centrifuged, washed with plenty of DI water, and dried overnight to produce PMMA spheres. A measure of 1.2 g of the obtained PMMA spheres was dispersed in a mixture of 50 mL of ethanol and 50 mL of water. Thereafter, 10 mL of ceric ammonium nitrate solution (3 g/L) was added to the mixture under stirring. Then, 0.6 g of dopamine hydrochloride, dissolved in 20 mL of DI water, was added quickly. The pH value was then adjusted to 8.5 with the addition of tris(hydroxymethyl)aminomethane (Tris-buffer), which was stirred for 24 h at room temperature. The dark gray suspension underwent filtration, repeated DI water washing, drying overnight at 60°C, and calcination at 650°C in an Ar atmosphere for 3 h to obtain the final sample of CeO₂-QDs.

2.2.2 Characterization

Transmission electron microscopy (TEM) (JEOL, JEM-2100, Tokyo, Japan) and field emission scanning electron microscopy (FE-SEM) (JEOL JSM-7800F, Tokyo, Japan) were applied to examine material morphologies. X-ray diffraction (XRD) patterns were collected using a Rigaku Ultima IV X-ray diffractometer applying Cu-K α radiation ($\lambda = 0.15418$ nm). XPS analysis was carried out on a VG-ESCALAB 220i-XL system with Al K radiation of 300 W and a pressure of approximately 3×10^{-9} mbar. A C 1s binding energy of 284.8 eV was used for the XPS peak correction (Luo et al., 2018). Fourier transform infrared spectroscopy (FT-IR) was performed on a TENSOR 27 spectrometer (Bruker, Germany), with the wave number ranging from 4,000 to 600 cm⁻¹.

2.2.3 Synthesis of PEA hydrogels

The PEA hydrogel was mixed with 10 wt% polyethyleneimine (Mw, approximately 70,000) and 10 wt% polyacrylic acid (Mw, approximately 240,000) in a volumetric ratio of 1:1 so as to achieve the best mechanical strength and adhesive strength according to the existing reports (Peng et al., 2021b). The blended mixtures were immediately submerged in liquid N₂ for 15 min, and then, water was removed by freeze-drying. Ultimately, the dried materials were ground into PEA powder.

2.2.4 Synthesis of the PEA@CeO₂-QDs hydrogel

Polyethyleneimine (Mn = 70,000, 50 wt%, x mL) was diluted to 10 wt%, and polyacrylic acid (Mn = 240,000, 25 wt%, 2x mL) was diluted to 10 wt% with DI water with different doses of CeO₂-QDs suspending in. The amount of CeO₂-QDs added to the solution was calculated according to the weight of the PEA hydrogel, and the drug loading concentrations were 25 mg/mL, 50 mg/mL, and 75 mg/mL. A measure of 10 wt% polyethyleneimine solution and 10 wt% polyacrylic acid solution with CeO₂-QDs were mixed evenly. The mixture was then immersed in liquid N₂ and lyophilized under the

same conditions as for PEA synthesis. PEA@nCeO₂-QDs refer to the PEA hydrogel loaded with n mg/ml CeO₂-QDs.

2.3 Mechanical tests

2.3.1 Tensile test

The bespoke clamps were used to conduct tensile testing on the dumbbell-shaped samples at a crosshead velocity of 3 mm min⁻¹ using a universal material testing machine (Instron 5300, United States). The tensile stress (σ_t) was determined using the following equation:

$$\sigma_t = \text{Load}/tw,$$

where t and w are the original specimen thickness and width, respectively. The difference in length from the starting gauge length was designated as the tensile strain (t). To guarantee the accuracy of the data, three specimens were evaluated for each experimental point.

2.3.2 Lap shear test

To evaluate the lap shear strength of the samples, thawed porcine skin was processed according to ASTM F2255 to generate adhesive samples with a 2.5 cm * 1 cm adhesive surface. Then, 50 mg of lyophilized PEA hydrogel powder or lyophilized PEA@CeO₂-QDs hydrogel powder was evenly distributed on the surface of the tissue coated with PBS, and pressure was applied for 1 min. The test was operated at a constant speed of 5 mm/min using a universal material testing machine (Instron 5300, United States). Then, the samples were pressed with a pressure of 8 kPa for 5 min at 25°C. The adhesion stress could be obtained by calculating $F_{\text{max}}/(wl)$, where F_{max} is the maximum force and w and l are the width and length of the adhesion area, respectively. To guarantee the accuracy of the data, three specimens for each condition were tested.

2.4 Rheological analysis, viscosity, and self-healing

2.4.1 Rheological analysis and viscosity

The hydrogel has distinguished rheological characteristics as a viscoelastomer. Rheological tests were performed at 37°C controlled by a Peltier system, utilizing a rheometer (Physica MCR 302, Anton Paar, Germany) fitted with a parallel-plate sample holder (PP25), the diameter of which was 25 mm. The rheometer was used to measure the time-dependent storage modulus (G') and loss modulus (G'') in an oscillatory time-scan test for 5 min at 30 measurement points with a steady strain amplitude of 1% and a frequency of 1 Hz, while a stable frequency was specified as 10 rad s⁻¹. Complementarily, the test was conducted after mixing the PEA freeze-dried powder with the PBS or CeO₂-QDs suspension for 30 s. In addition, G' and G'' of samples were monitored at an invariant angular frequency (10 rad s⁻¹) at 25 measurement points with applied shear strain levels ranging from 0.001% to 100% in an oscillatory amplitude sweep test, and the flow point of the hydrogel was calculated at the point of intersection of G' and G'' . G' and G'' were also determined using the angular frequency sweep measurement with 1% strain at 16 measurement points. The viscosity of the sample hydrogel was measured using the above device at the same ambient temperature.

2.4.2 Experiments on macroscopic self-healing

To create the columnar hydrogel with a length of 2.5 cm and a diameter of 0.5 cm, the PEA hydrogel and PEA@75CeO₂-QDs were utilized, respectively. The hydrogel was divided into four segments, which were then joined and incubated at 37°C for 5 min to allow the hydrogel to self-heal and reestablish its full columnar shape. Each hydrogel segment could withstand its weight and self-heal at the broken ends. The hydrogel was also bent into a U shape, and each of the aforementioned morphologies was documented and photographed simultaneously.

2.5 Swelling and degradation behavior

The freeze-dried hydrogel samples were weighed (W_0) and then immersed in 3 mL of PBS (pH 7.4) at 37°C for 24 h to reach equilibrium. The hydrogel was expanded, the weight of which was measured as W_1 after the surplus solution was absorbed by filter paper from the hydrogel surface. The swelling ratio of the hydrogel was ultimately obtained using the following formula:

$$\text{Swelling ratio (\%)} = (W_1 - W_0) / W_0 \times 100\%.$$

These samples were subsequently submerged in 5 mL of PBS (0.01 M, pH = 7.4) while being incubated at 37°C for 1, 2, 3, 5, 7, and 10 days, individually. Following the separation of the samples from PBS and lyophilization, their ultimate weight (W_t) was calculated. The experiment was carried out in triplicate. The amount of degradation *in vitro* was calculated using the following formula:

$$\text{Residual (\%)} = W_t / W_0 \times 100\%.$$

2.6 SOD, CAT, and T-AOC enzyme mimic activities of the PEA@CeO₂-QDs hydrogel

Superoxide dismutase (SOD), catalase (CAT), and total antioxidant capacity (T-AOC) activities were evaluated using an enzymatic calibrator (Thermo Scientific, Multiskan GO, United States) to determine the antioxidant levels.

The primary H₂O₂ scavenging enzyme, CAT, is crucial to the system for removing H₂O₂. Following the directions provided in the manual for mixing the CAT working medium with the specimen, the hydrogen peroxide level of ultraviolet light at 240 nm after 1 min was promptly ascertained at room temperature. The CAT enzyme activity is inversely correlated with the hydrogen peroxide concentration. SOD could participate in the superoxide anion (O₂⁻) disproportionation reaction to release H₂O₂ and O₂. O₂⁻ originates from the reaction involving xanthine. Xanthine oxidase can be used to diminish nitrogen blue tetrazolium to yield blue methanogenesis, which absorbs at 560 nm. By scavenging O₂⁻, SOD hinders the synthesis of blue methanogenesis.

The total antioxidant level in the examined objects consists of antioxidants and antioxidant enzymes. The total antioxidant capability is indicated by the ability to reduce Fe³⁺-tripyrildiazine (TPTZ) to generate blue Fe²⁺-TPTZ in an acidic environment. Each SOD, CAT, and T-AOC activity test was repeated three times.

2.7 Cytocompatibility assay for the PEA@CeO₂-QDs hydrogel

CCK-8 was used to figure out the cell compatibility in L929. The leaching liquor of the PEA hydrogel, PEA@25CeO₂-QDs, PEA@50CeO₂-QDs, and PEA@75CeO₂-QDs were used to cultivate the fibroblasts for 24, 48, and 72 h. L929 cells were transferred at a density of 2,000 cells per well in 96-well plates and then cultured at 37°C in a 5% CO₂ atmosphere in Dulbecco's modified Eagle's medium (DMEM) containing 10% fetal bovine serum (FBS) and 1% penicillin-streptomycin. Live cells were identified by CCK-8 after incubation in the leaching liquor, implementing a microplate reader at OD 450 nm (Detie, HBS-1096A, China) at 37°C for 2 h.

2.8 Bacterial cultivation and antibacterial effect assessment of the PEA@CeO₂-QDs hydrogel

The Institutional Review Board of the Qingdao University School of Dentistry granted permission for the experimental use of two bacterial pathogens, *S. aureus* cultured in tryptic soy broth (TSB), while *E. coli* was grown in Luria broth (LB). The antibacterial property of PEA@CeO₂-QDs was assessed, while the bacterial growth activity was measured by co-culturing the suspension of the bacterium and PEA hydrogel, PEA@25CeO₂-QDs, PEA@50CeO₂-QDs, and PEA@75CeO₂-QDs. A fresh colony was chosen and incubated on a shaker at 200 rpm overnight at 37°C.

2.8.1 Time-kill assay

This test involved *S. aureus* and *E. coli* exposed to PEA loaded with different concentrations CeO₂-QDs over time. A mixture of 100 μL of the solution comprising PBS and an inoculum of the tested pathogens (10 μL) at a concentration of 10⁶ CFU/mL was inoculated on the surface of the hydrogel in each group. The samples that did not contain any PEA or CeO₂-QDs served as the negative controls. A microplate reader was used to measure the optical density at a wavelength of 630 nm to monitor the growth of different bacterial species during the course of the bacterial culture. After co-cultivation with the PEA hydrogel, PEA@25CeO₂-QDs, PEA@50CeO₂-QDs, or PEA@75CeO₂-QDs, the surface of each group hydrogel was rinsed off repeatedly with PBS, and then, the obtained bacterial suspension was diluted 50–2,000 times with PBS before being spread uniformly onto TSB or LB agar plates and incubated at 37°C for 24 h.

2.8.2 SEM inspection of the bacterial morphology

The process for co-cultivation is the same as previously described. The absorbance of the bacterial solution at the wavelength of 630 nm was adjusted to 0.1 before counting CFU and co-cultivation, and the bacterial liquid could provide blank controls as well. At room temperature, the bacterial suspension was centrifuged at 0.5 cc for 15 min at 6,000 rpm. The resulting pellet was cleaned three times with sterile PBS before being fixed for 2 h with 2.5 wt% glutaraldehyde. SEM was performed with gold spraying on the surface of the sample.

2.9 Inflammatory and anti-inflammatory gene expression *in vitro*

Raw 264.7 macrophages (murine leukemia monocyte-macrophage cell line, ATCC: TIB-71) were cultured in Dulbecco's modified Eagle's medium supplemented with fetal bovine serum (10%, *v/v*), without penicillin (100 U/mL) and streptomycin. *Porphyromonas gingivalis* LPS ($1 \mu\text{g mL}^{-1}$) was introduced to stimulate RAW 264.7 cells for 24 h, which were then seeded into 6-well plates with the leaching liquor of the PEA hydrogel, PEA@25CeO₂-QDs, PEA@50CeO₂-QDs, and PEA@75CeO₂-QDs for an additional 24 h. LPS-stimulated cells without being treated with leaching liquor samples played the role of negative controls. The concentration of RAW 264.7 cells was maintained at 10^6 cells per mL. Using real-time PCR, we measured M1 phenotype macrophage-associated cytokines (IL-1 β , IL-6, and TNF- α) and M2 phenotype macrophage-associated cytokines (IL-10, Arg-1, and TGF- β), simultaneously standardizing the data to the housekeeping gene β -actin on RAW 264.7 cells, a representative *in vitro* model of inflammation. The experiment was repeated in triplicate. The $2^{-\Delta\Delta\text{CT}}$ approach was applied to determine the gene expression levels of each sample.

2.10 Statistical analysis

Each experiment was repeated at least three times. GraphPad was used to perform the statistical analysis. The mean and standard deviation are used as representations for the statistical analysis of all data. Using one-way ANOVA and Tukey's *post hoc* test to compare the group mean values, significant effects of factors were found at *p*-values less than 0.05 (* *p* < 0.05, * * *p* < 0.01, * * * *p* < 0.001, and * * * * *p* < 0.0001).

3 Results and discussion

3.1 Preparation and characterization of the CeO₂-QDs, PEA hydrogel, and PEA@CeO₂-QD hydrogel

Figure 1 features a comprehensive description of the preparation of CeO₂-QDs and PEA@CeO₂-QDs hydrogels. CeO₂-QDs are successfully synthesized using PMMA as a hard template and dopamine as the chelating agent. PMMA is removed by high-temperature calcination, and CN scaffolds anchoring highly dispersed CeO₂-QDs are obtained. As shown in Figure 2A, CeO₂-QDs show macroscopical powder morphology. The homogeneous PEA freeze-dried powder offers an increased surface area that could enable the sample to quickly gel upon exposure to water. The SEM and TEM images given in Figures 2B,C show that CeO₂-QDs demonstrate a 3D honeycomb texture abundant with interconnected pores, which will provide a higher exposed surface, benefitting the contact with PEA. Ultra-small CeO₂-QDs with a size of approximately 1.5–2.5 nm are uniformly dispersed on the scaffold, as shown in the HR-TEM image in Figure 2D.

The XRD pattern (Figure 2E) reveals that the diffraction peak corresponding to CeO₂ could barely be observed in the CeO₂-QDs.

This could be due to the extremely small particle and its low long-range crystallinity, which highlights again the high dispersion state of the ultra-small CeO₂ nanoparticles.

XPS spectra are analyzed to identify the chemical state of Ce. Figure 2F shows that C, N, O, and Ce are presented for the sample of CeO₂-QDs. According to the deconvolution of the N 1s XPS peak, the N species contains 17.0% of pyridinic N (398.2 eV), 47.8% of pyrrolic N (400.8 eV), and 25.3% of graphitic N (402.6 eV) (Figure 2G). Lattice O (O_{lat}) with a peak at 529.8 eV, surface O (O_{sur}) with a peak at 532.5 eV, which accounts for 65.3% of O species, and the CN surface oxygen functional group with a peak at 534.6 eV could be observed in the O 1s XPS spectra of CeO₂-QDs (Figure 2H). It has been confirmed that the amount of oxygen vacancies closely correlated to the content of Ce³⁺ O_{sur} (Geng et al., 2016; Brugnoli et al., 2018; Chakrabarty et al., 2021; Grinter et al., 2021; Yadav and Singh, 2021). The Ce 3d XPS spectra could be divided into eight peaks after deconvolution, of which the peaks designated V' and U' correspond to Ce³⁺, while V, V'', V''', U, U'', and U''' symbolize the existence of Ce⁴⁺ (Figure 2I). The Ce³⁺ percentage $\text{Ce}^{3+}/(\text{Ce}^{3+} + \text{Ce}^{4+})$ of CeO₂-QDs is 33.83%, as calculated. Consequently, the Ce³⁺ percentage in CeO₂-QDs is more adequate than that of other CeO₂ nanoparticles with merely antibacterial or anti-inflammatory features (Xia et al., 2020; Wang Y. et al., 2021; Zhuo et al., 2021), suggesting oxygen vacancy-rich features for CeO₂-QDs, which will play an important role in promoting the antibacterial activity directly.

FT-IR characterization is further carried out to elaborate the cross-linking mechanisms of the PEA@CeO₂-QDs hydrogel. As shown in Figure 2J, the amine group peaks and carboxylic acid peaks in the PEA@CeO₂-QDs hydrogel shift from 1,563 cm⁻¹ to 1,560 cm⁻¹ and from 1,635 cm⁻¹ to 1,630 cm⁻¹, respectively. After the addition of CeO₂-QDs, the typical amine group and carboxyl peak shifts could be attributed to the newly created hydrogen bond. The lack of new characteristic absorption peaks in the PEA@CeO₂-QDs hydrogel suggests that the PEA hydrogel is still cross-linked via hydrogen bonds and electrostatic interactions rather than a newly created covalent bond.

PEA@CeO₂-QDs powder could be gelled *in situ* once placed on the surface of the substrate wetted by DI water or PBS. The inset of Figures 2K–N shows that PEA, PEA@25CeO₂-QDs, PEA@50CeO₂-QDs, and PEA@75CeO₂-QDs hydrogels are all well gelled on the wet cover glass. The SEM images in Figure 2K show that the PEA hydrogel surface is relatively smooth, which is in accordance with earlier research (Peng et al., 2021a). Figures 2L–N show that there are plenty of particles embedded incompletely on the surface of the PEA@CeO₂-QDs hydrogel, and the density of the particles increases with the increase in the concentration of the added CeO₂-QDs, which facilitates the release of CeO₂-QDs. As the hydrogel deteriorates, more CeO₂-QDs particles could be progressively exposed and released into the wound.

3.2 Mechanical properties of the PEA@CeO₂-QDs hydrogel

Properties like tensile qualities, dependable adhesion, and significant mobility are required for dressings placed on moist

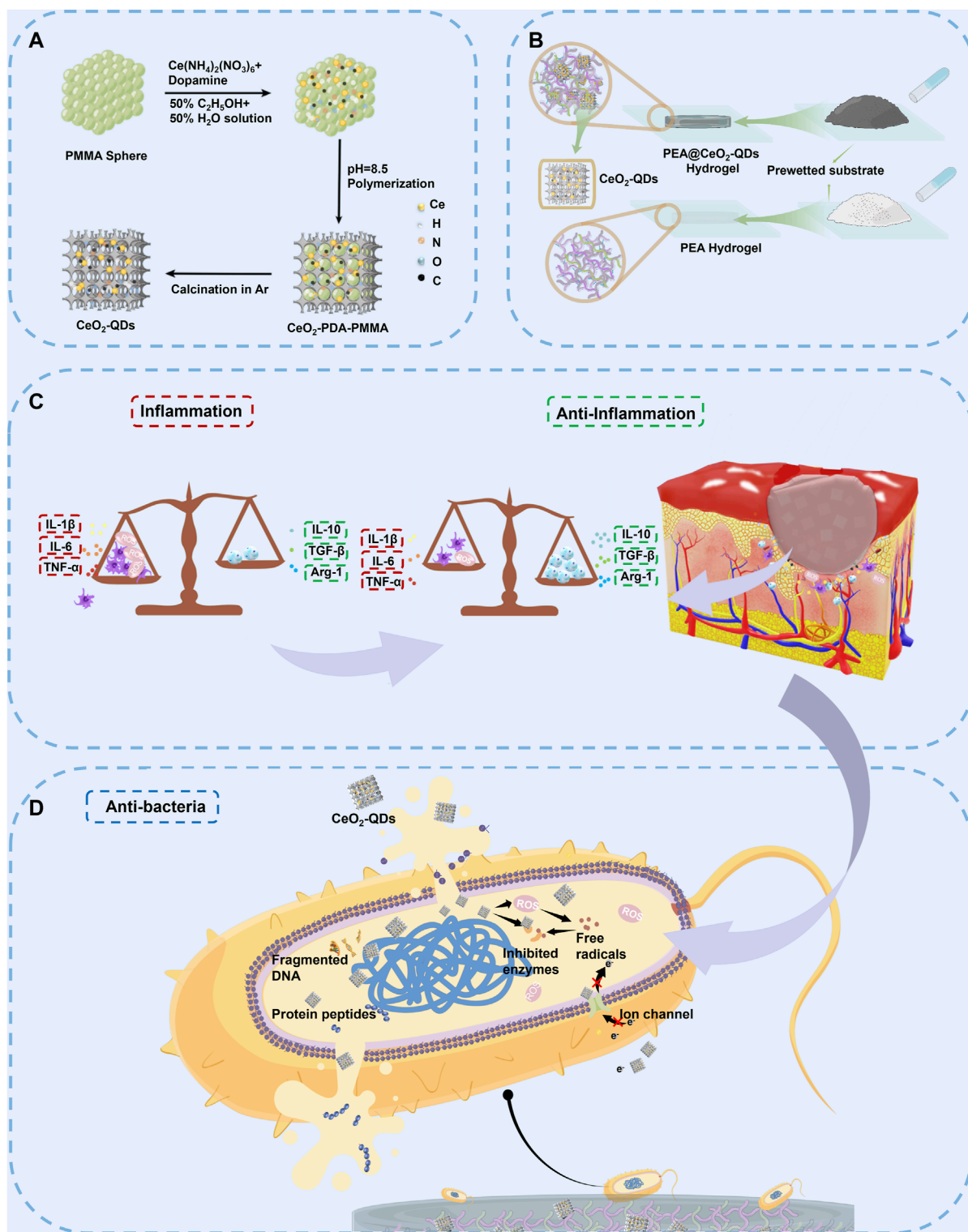
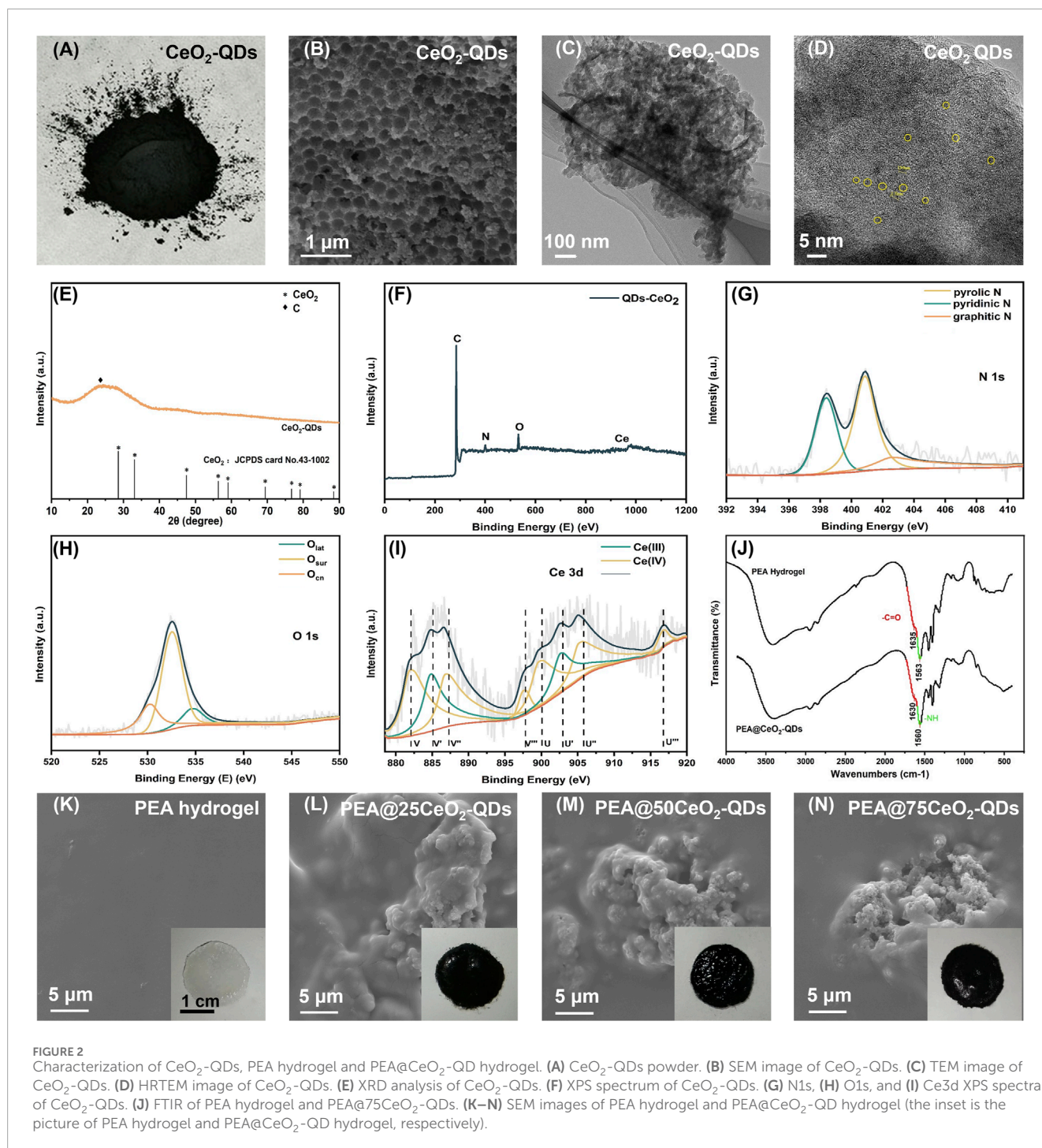


FIGURE 1 Schematics of the synthesis, anti-inflammatory mechanism, and antimicrobial mechanism of the PEA@ CeO_2 -QDs hydrogel. **(A)** Synthesis of CeO_2 -QDs. **(B)** Synthesis of PEA and PEA@ CeO_2 -QDs hydrogels. **(C)** Anti-inflammatory mechanism of the PEA@ CeO_2 -QDs hydrogel. Benefited by the higher proportion of Ce^{3+} in the CeO_2 -QDs, more ROS could be produced to kill *S. aureus* and *E. coli*. **(D)** Antimicrobial mechanism of PEA@ CeO_2 -QDs hydrogel. Moreover, the presence of Ce^{4+} can clear the excessive ROS and relieve oxidative stress, thus inducing macrophage M2-type polarization to play an anti-inflammatory role.

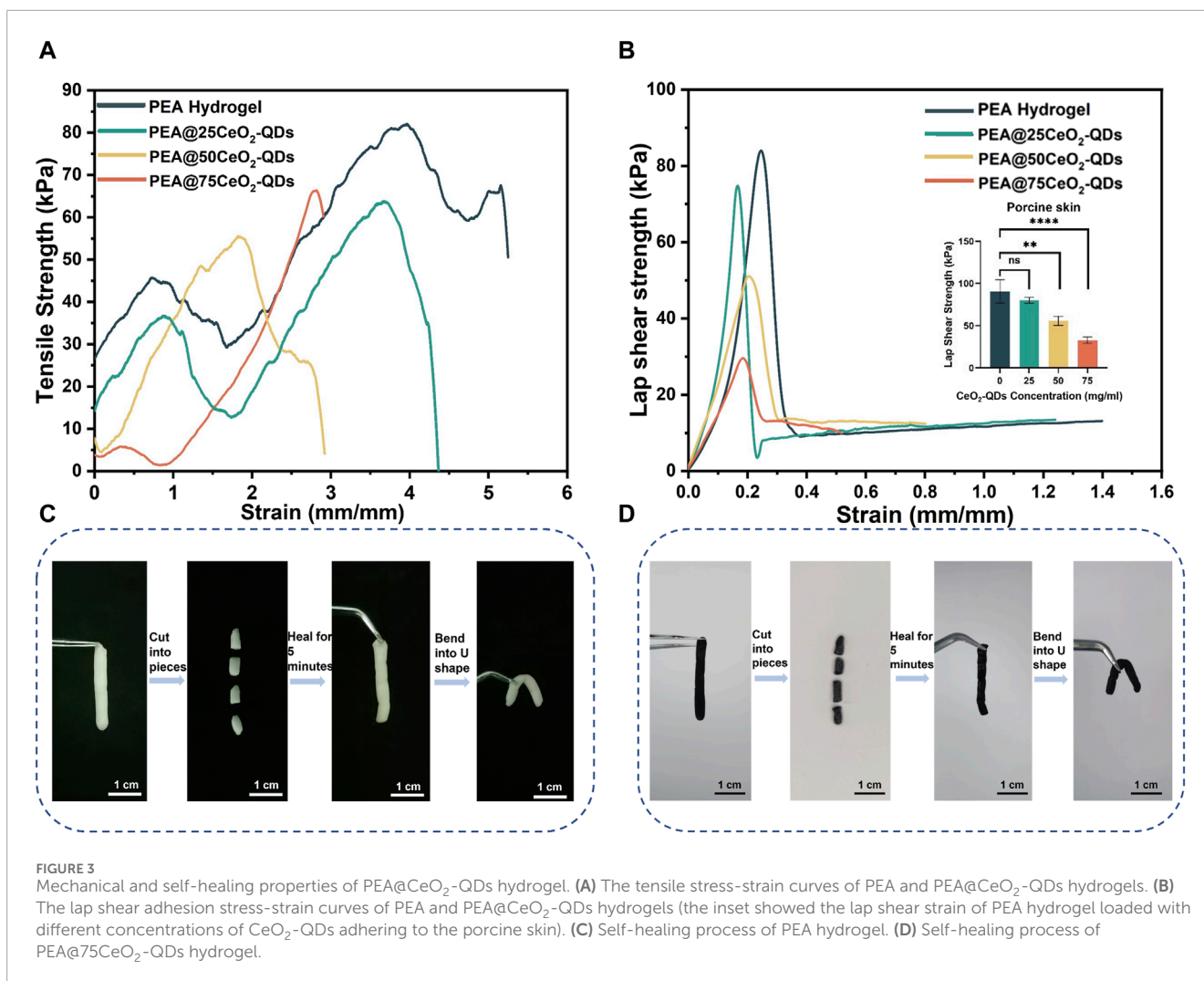


tissues. The mechanical performances of the PEA hydrogel are primarily affected by electrostatic and hydrogen-bonding interactions.

3.2.1 Tensile test

The tensile properties are shown in **Figure 3A**. The maximum tensile strength of the hydrogel decreases from 80 kPa to 64 kPa and 65 Kpa when the concentration of CeO₂-QDs increases from 0 to 25 mg/mL and 50 mg/mL, respectively. The maximum tensile strength of the hydrogel is 55 kPa at a CeO₂-QDs concentration of

75 mg/mL, which is 31.25% less than that of the pure PEA hydrogel. In the bargain, the tensile strain at the fracture also steadily decreases from more than 500% to 400%, 300%, and 200% when the loading CeO₂-QDs concentration increases. PEA, PEA@25CeO₂-QDs, and PEA@50CeO₂-QDs hydrogels all display acceptable tensile qualities, while the tensile properties of the PEA@75CeO₂-QDs hydrogel are significantly compromised. Jia et al. demonstrated that the maximum stress and tensile strain at the break in the longitudinal tensile test of the porcine gastric wall mucosa were comparable to those of the PEA hydrogel (Jia et al., 2015). The results of this



research support the therapeutic application of PEA as a wound dressing for the gastric wall mucosa because it resists rupture even when the mucosa stretches and contracts. Even though the increasing loading of CeO₂-QDs has a negative effect on the tensile characteristics of the PEA hydrogel, the self-healing ability of the hydrogel allows the repair of the tensile fracture interface.

As shown in Figures 3C,D, the PEA hydrogel and PEA@75CeO₂-QDs hydrogel are utilized to create a columnar hydrogel with a length of 2.5 cm and a diameter of 0.5 cm. The PEA columnar hydrogel and the PEA@75CeO₂-QDs hydrogel are both sliced into four segments and then incubated for 5 min at 37°C. The boundary between segments of the two groups was blurred, and when one end is picked up using forceps, there is no separation of other segments. The thorough connection at the fractured ends of the two repaired hydrogel remains intact even after being twisted into a U shape. Referring to the newly created hydrogen bond (Figure 2J), we assume that the electrostatic force and hydrogen bonding are accountable for the great self-healing efficiency of the PEA hydrogel and PEA@75CeO₂-QDs hydrogel. Furthermore, the PEA and PEA@CeO₂-QDs hydrogels are viscoelastic, additionally suggesting that they have good wound adaptability, which is a crucial aspect of wound dressing.

3.2.2 Lap shear adhesion and self-healing

In the present study, it is verified that the PEA hydrogel has superior adhesion on the surface of the porcine skin. Figure 3B shows that when the CeO₂-QDs concentration increased from 0 mg/mL to 50 mg/mL, the maximum lap shear stress of the hydrogel notably steadily decreased from 75 kPa to 73 kPa and 47 kPa. Nevertheless, for the PEA@75CeO₂-QDs hydrogel, the maximum lap shear stress is approximately 56 kPa. Additionally, the strain of the hydrogel gradually decreases from 4.6 to 2.3, 2.2, and 0.8 mm/mm when it is entirely dislocated from the porcine skin. In other words, a higher loading amount of CeO₂-QDs causes a trend toward the displacement of the PEA hydrogel. Peng et al. discovered that the *in situ* PEA hydrogel was stably bonded to the substrate and then progressively permeated the substrate network. Even though the surface of the PEA hydrogel was removed, a small amount of residue remained on the substrate surface (Peng et al., 2021b). Likewise, in the lap shear experiment, the finding indicates the presence of PEA hydrogel remnants at the separation interface. Considering the self-healing experiment (Figures 3C,D), after the PEA@CeO₂-QDs hydrogel separates from the substrate at the wound, the self-healing properties allow the interface to recontact, thereby

enabling the PEA@CeO₂-QDs hydrogel to shield the wound once again.

3.3 Rheological analysis

The elastic modulus (G') and loss modulus (G'') of the hydrogel in each group are evaluated in the strain range from 0% to 100% to assess the viscoelasticity of the hydrogel. G' stands for the elasticity and degree of cross-linking, whereas G'' stands for the viscosity. The hydrogel structure could start to collapse locally or integrally at the intersection before $G' < G''$. When G'' varies from 8,000 Pa to 2,500 Pa in the PEA hydrogel, G' changes from 17,500 Pa to 2,500 Pa. Furthermore, the hydrogel consistently maintains $G' > G''$ when the strain ranges from 0% to 100%, indicating that the gel framework is robust enough from being destroyed. However, as shown in Figures 4A–D, the G' range is lowered to 8,500–600 Pa, 5,700–500 Pa, and 5,000–400 Pa in PEA@25CeO₂-QDs, PEA@50CeO₂-QDs, and PEA@75CeO₂-QDs, respectively. The G'' is 4,700–600 Pa, 2,500–500 Pa, and 3,200–700 Pa, respectively. Both G' and G'' are reduced to some extent when the doping concentration of CeO₂-QDs increases. The intersection of G' and G'' is recognized as the flow point in the linear viscoelastic range. The flow points of PEA@25CeO₂-QDs and PEA@50CeO₂-QDs occur in the strain range of 21.7%–31.8%, and the flow points of the PEA@75CeO₂-QDs emerge in the strain range of 31.8%–46.7%. The cross-linked structure of the PEA hydrogel collapses under moderate strain as a consequence of the addition of CeO₂-QDs.

We further determine that the hydrogel of each group maintains $G' > G''$ at a lower angular frequency (Supplementary Figure S1), according to the rheological curve of the PEA hydrogel and PEA@CeO₂-QDs in the angular frequency range of 0.1–100 rad s⁻¹ under 1% strain. Additionally, the oscillation time scan data reveal that after 300 s of gelation, the G' value of the PEA hydrogel and the hydrogel loaded with CeO₂-QDs remains constant (Supplementary Figure S2), but over time, both G' and G'' tend to be stable, and no suspicious rearrangement takes place. As shown in Supplementary Figure S3, the hydrogel viscosity change curve for each group has a similar tendency in which the viscosity decreases abruptly at low shear rates before stabilizing at higher shear rates. In addition, as the concentration of CeO₂-QDs increases in each group, the shear rate is low; however, the viscosity is increased. Additionally, even if the fracture occurs, the self-healing ability of the hydrogel allows the fracture ends to mend immediately. Electrostatic force, along with weak hydrogen bonds, plays an essential role in the rheological characteristics of the PEA@CeO₂-QDs hydrogel.

3.4 Swelling and degradation

Swelling could reflect the potential of the hydrogel to suck up the wound exudates (Wang H. et al., 2021). As shown in Figure 4E, the PEA hydrogel swells at a rate of 117.1 ± 0.8% over the course of 24 h, while PEA@25CeO₂-QDs, PEA@50CeO₂-QDs, and PEA@75CeO₂-QDs hydrogels swell at rates of 119.4 ± 1.6%, 117.6 ± 2.9%, and 117.6 ± 1.5%, respectively. No significant distinction was observed between each group, implying that the addition of CeO₂-QDs has

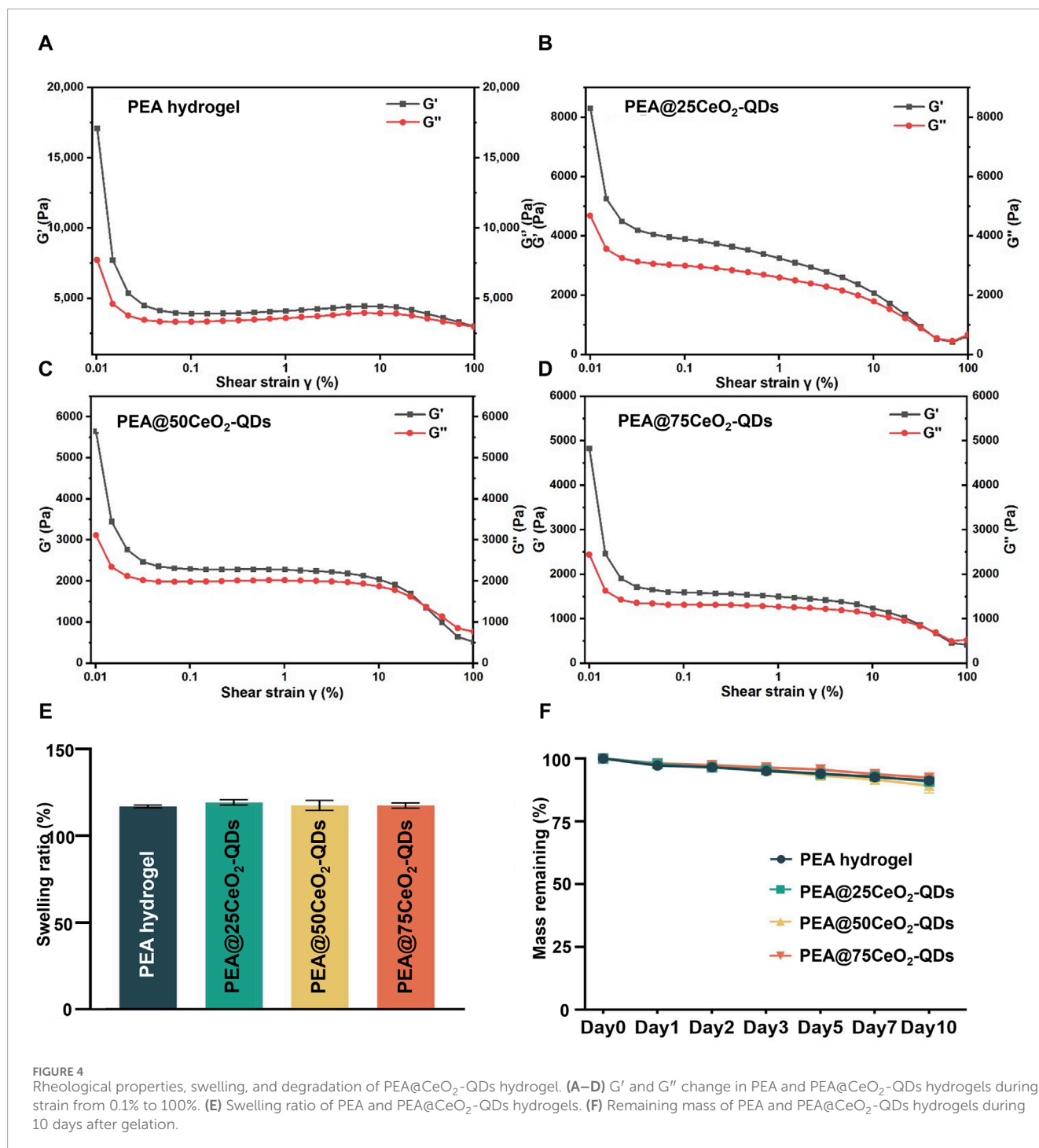
no negative effect on the excellent swelling rate of the PEA hydrogel. McColl et al. found that cell migration and re-epithelialization were aided by the wound site being moderately wet rather than macerated (McColl et al., 2007). PEA and PEA@CeO₂-QDs hydrogels serve as excellent candidates for wet tissue wound dressings because they are capable of collecting exudates during wound repair and gland secretion.

Hydrogel wound dressings are required to have appropriate degradation qualities for the regeneration of epithelial tissue to promote the growth of cells and blood vessels and minimize the negative effects of degradation byproducts (Cao et al., 2021). However, the biodegradable hydrogel was more likely to lead to multicellular aggregation than the non-degradable hydrogel, ultimately resulting in uneven morphology at the area of injury (Carey et al., 2015; Taubenberger et al., 2019). Figure 4F shows that the mass residual rates of PEA and PEA@CeO₂-QDs hydrogels on day 10 are 91.2% ± 1.1%, 90.8% ± 1.2%, 89.2% ± 3.0%, and 92.4% ± 0.8%, respectively. Additionally, only approximately 10% of each group of hydrogel degrades within 10 days, given that both PEA and PEA@CeO₂-QDs hydrogels could continue to exist in a stable state, while the additional CeO₂-QDs have no significant effect on the degradation kinetics. This proper degradation speed could avoid multicellular aggregation and facilitate the wet tissue wound restoration to healthy physiological morphology.

3.5 The enzyme-mimetic activity of PEA and PEA@CeO₂-QDs hydrogels

SOD enzymes can remove •OH and O₂⁻, which can be completed by Ce³⁺. In contrast, CAT enzymes can undergo a reduction reaction when they break down H₂O₂, which is similar to the electron conversion of Ce⁴⁺ to Ce³⁺. Ce³⁺ can convert O₂⁻ to H₂O₂, which has a bactericidal effect (Singh et al., 2011; Ju et al., 2021; Yadav and Singh, 2021).

By XPS, we determine that the Ce³⁺/Ce³⁺+Ce⁴⁺ ratio in CeO₂-QDs is 33.83%, which is much greater than the Ce³⁺ ratio in larger CeO₂ nanoparticles (Figure 2I). The loss of oxygen atoms from the lattice can result in oxygen vacancy due to the reduction in Ce⁴⁺. A higher Ce³⁺ ratio, or more oxygen vacancies, has been demonstrated to correspond to SOD enzyme mimic activity (Li et al., 2023; Luneau et al., 2023), while a lower Ce³⁺ ratio implies a higher CAT mimic activity (Chen and Stephen Inbaraj, 2018; Yadav et al., 2022). Tiny particle-sized CeO₂-QDs have an increased fraction of Ce³⁺ than large particle-sized CeO₂ nanoparticles due to the size effect, implying that CeO₂-QDs exhibit an enhanced antibacterial effect (Xue et al., 2011; Kilic et al., 2021). At the same time, Ce³⁺ exhibits SOD enzyme mimic activity via eliminating ROS such as H₂O₂ while converting to Ce⁴⁺ (Nelson et al., 2016; Bezkrvnyy et al., 2022). Using CAT mimic activity assays, SOD mimic activity assays, and T-AOC assays, the enzyme mimic activity of the PEA@CeO₂-QDs hydrogel is demonstrated in this study. The data collected reveal that the CAT mimic activity, SOD mimic activity, and T-AOC of the hydrogel-leaching liquor significantly improved with the increase in the CeO₂-QDs concentration from 0 mg/mL to 75 mg/mL (Figures 5A–C). The PEA@75CeO₂-QDs hydrogel group shows stronger CAT mimic activity, SOD mimic activity, and T-AOC.



3.6 Cytocompatibility of PEA and PEA@CeO₂-QDs hydrogels

The results given in Figure 5D show that no cytotoxicity is detected for the PEA@75CeO₂-QDs hydrogel during 72 h. Each group has considerable proliferation promotion activity at 72 h, and the effect is amplified as the CeO₂-QDs concentration increases. High biocompatibility is exhibited by the majority of CeO₂ nanoparticles and nanocomposites (Hu et al., 2020; Naidi et al., 2021a; Sukhanova et al., 2022). The biocompatibility of CeO₂-QDs

is significantly better than that of CeO₂ with a particle size greater than 10 nm or even 20 nm (Liman et al., 2019; Naidi et al., 2021a). Despite a high increase in CeO₂-QDs addition, L929 cells demonstrate good biological activity and increased cell proliferation. This variation could be spurred by a distinction in CeO₂ particle size. Ren et al. discovered that proliferative activity was also present in CeO₂ nanoparticles of size 8.1 ± 4.6 nm (Ren et al., 2022). Moreover, as cultivated cells grow with metabolism and passage, ROS levels continuously increase, and oxidative damage gradually worsened (Wang et al., 2019). By eliminating excess ROS, CeO₂-QDs in

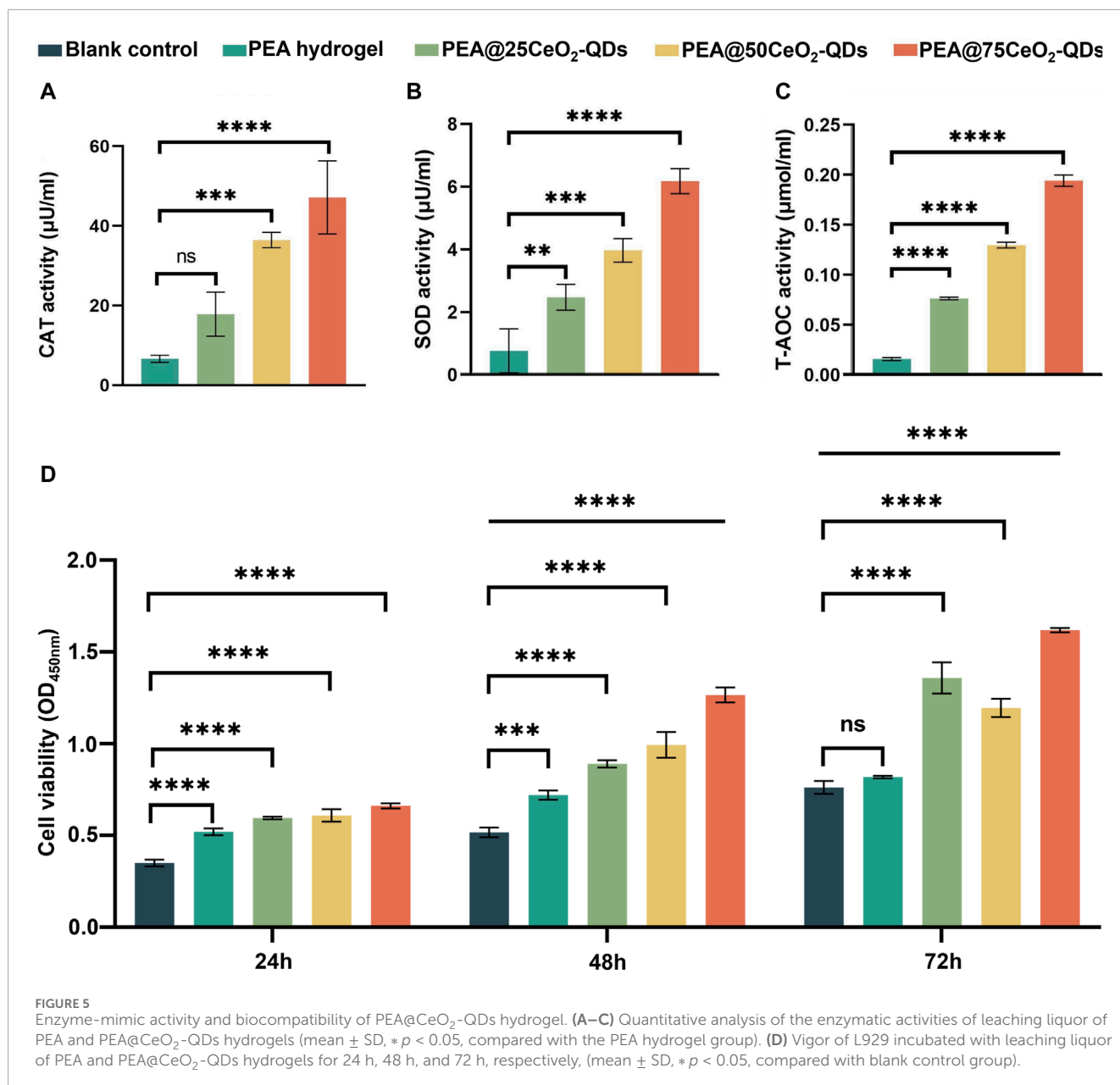


FIGURE 5 Enzyme-mimic activity and biocompatibility of PEA@CeO₂-QDs hydrogel. (A–C) Quantitative analysis of the enzymatic activities of leaching liquor of PEA and PEA@CeO₂-QDs hydrogels (mean ± SD, **p* < 0.05, compared with the PEA hydrogel group). (D) Vigor of L929 incubated with leaching liquor of PEA and PEA@CeO₂-QDs hydrogels for 24 h, 48 h, and 72 h, respectively, (mean ± SD, **p* < 0.05, compared with blank control group).

the PEA@CeO₂-QDs hydrogel prevent ROS springing from the degradation or destruction of DNA, protein, or lipid-damaging cells (Mahapatra et al., 2017). According to Van et al., QDs principally entranced cells through the processes of phagocytosis, pinocytosis, and micropinocytosis (Van Lehn et al., 2013). They additionally noted that the diameter of the particle was inversely correlated with the rate when QDs penetrated and left the cell (Van Lehn et al., 2013). Therefore, the size of QDs is critical to their biocompatibility. Greater potential for irreversible damage to the cell membrane during the process of breaching the membrane was associated with larger nanoparticles and, thus, improved the likelihood of damaged cells dying (Greish, 2010; Sukhanova et al., 2022). The excellent cytocompatibility enables the PEA@CeO₂-QDs hydrogel as a competitive candidate to function as an antibacterial and anti-inflammatory dressing for wet tissue.

3.7 Antibacterial properties of the PEA@CeO₂-QDs hydrogel

Wet tissues, such as the esophagus, digestive tract, and mouth mucosa, originally conduct functional activities in an environment full of bacteria. With more than 770 varieties of bacterial colonies, the oral cavity is one of the most intricate bacterial reservoirs in the human body (Kitamoto et al., 2020). Apart from this, anachoresis is the process by which diseased or damaged tissue absorbs germs from the circulation at the site of the injury. Thus, the wound is more vulnerable to bacterial infection owing to anachoresis. *S. aureus* and *E. coli* serve as critical components and common pathogenic microorganisms isolated from the infected wounds. Bacteria may enter the wound and reproduce there, even disrupting the homeostasis and precipitating wound infection.

In this study, Gram-positive and Gram-negative microorganisms are represented by *S. aureus* and *E. coli*, respectively (Figure 6A). The representative growth curves of *E. coli* and *S. aureus* over 24 h are shown in Figures 6B,C. Significant growth inhibition is observed at 2 h in PEA and PEA@CeO₂-QDs hydrogels. Although the growth curves of both *E. coli* and *S. aureus* disclose a slight growth tendency after 2 h of co-culture, PEA@CeO₂-QDs still manifest an inhibition effect compared to the PEA group. The inhibitory impact becomes prominent as the drug concentration increases. Both PEA@50CeO₂-QDs and PEA@75CeO₂-QDs hydrogels reveal the strongest bactericidal effect, and no significant difference was observed between them. The growth curves of *S. aureus* and *E. coli* were altered over 24 h; the following factors could be utilized to clarify the variation. Initially, due to the starting bacterial population being relatively small and the hydrogel abilities of adherence and even inclusion to bacteria, the growth curves of *S. aureus* and *E. coli* in the PEA and PEA@CeO₂-QDs trend downward within 0–2 h. Ce³⁺ and copious oxygen vacancies in CeO₂ nanoparticles are speculated to cause damage to the cell walls of both Gram-positive and Gram-negative bacteria, including some multi-resistant strains, leading to antibacterial effects (Babu et al., 2014; Kumar et al., 2018). During the process of Ce³⁺ transformation into Ce⁴⁺, H₂O₂, a critical member of ROS, is generated. Small-sized CeO₂ displayed dose-dependent antibiotic activity (Arumugam et al., 2015; Naidi et al., 2021b). Therefore, an increase in the CeO₂-QDs concentration inevitably leads to an elevation in the exposed CeO₂-QDs particles on the hydrogel surface, providing theoretical evidence for the fact that PEA@50CeO₂-QDs and PEA@75CeO₂-QDs hydrogels manifest preferable bactericidal effects from the beginning.

During the 2 h–6 h of co-culture, although the antibacterial effects have been partially revealed, the *E. coli* and *S. aureus* growth curves display an upward but subtle trend in contrast to the initial 0–2 h. On the surface of the PEA hydrogel, the high-level CeO₂-QDs concentration with Ce³⁺ is exposed more. However, when Ce³⁺ is transformed into Ce⁴⁺ to execute sterilization, Ce⁴⁺ at a certain concentration could decompose H₂O₂ to produce H₂O and O₂ and, at the same time, be reduced to Ce³⁺. Therefore, in this process, the bactericidal effect will be discounted. Because the degradation rate of the PEA hydrogel is not so fast (Figure 4F), the fresh Ce³⁺ supplement will not be exposed massively for a short period of time. Last but not least, the growth curves of *S. aureus* and *E. coli* essentially attain steady states at concentrations of 50 mg/mL and 75 mg/mL, respectively from 6 h to 24 h. The above results could be explained by the deterioration of the PEA hydrogel on the surface and exposure of CeO₂-QDs. Based on the material properties of penetrating bacterial walls and releasing ROS, CeO₂-QDs could cause damage to bacterial cell walls and membranes (Pisal et al., 2019), resulting in peptide chain loss, enzyme activity reduction, DNA fragmentation, and electron transport interception (Kumar et al., 2018; Nadeem et al., 2020). The aforementioned behaviors could directly trigger the mortality or severe injury of bacteria or impede bacterial reproduction, hence exerting an antibacterial effect.

Figures 6D,E show representative images of CFU counts for *S. aureus* and *E. coli*, which reflects the antibacterial effect of the PEA@CeO₂-QDs hydrogel more intuitively. An essential sign of bacterial survival is the integrity of the cell membrane. SEM images

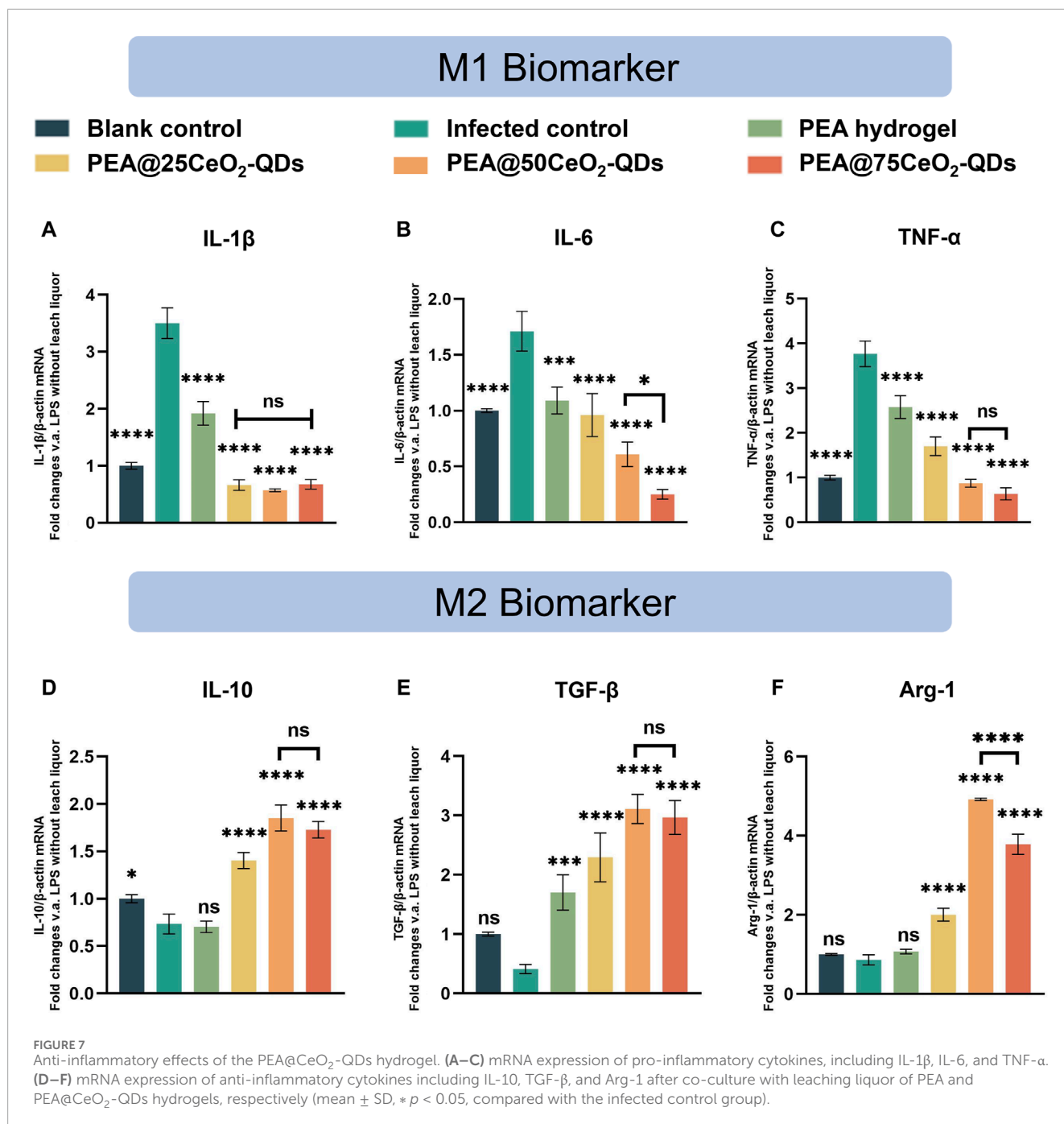
are used in this investigation to examine how the morphology of *S. aureus* and *E. coli* changes after 24 h of co-cultivation on the surfaces of PEA and PEA@CeO₂-QDs hydrogels. Figures 6F,G depict that the morphology of bacteria is complete and smooth on the PEA hydrogel. Nonetheless, the bacteria undergo varied degrees of deformation and collapse on the surface of the PEA@CeO₂-QDs hydrogel. The amount or percentage of malformed bacteria and the concentration of CeO₂-QDs in each field essentially follow the same pattern as the bacterial growth curve of *S. aureus* or *E. coli*. This agrees with the assumption that the cell wall and membrane of the bacteria are destroyed by CeO₂-QDs.

The production of ROS represents the crucial mechanism by which CeO₂ exerts its bactericidal effects. Kannan et al. discovered that after penetrating bacteria, CeO₂ inactivated enzymes in cells, creating ROS and leading to bacterial cell death (Kannan and Sundrarajan, 2014). For CeO₂-QDs, the much smaller size facilitated the entry of CeO₂, leading to a bactericidal effect by converting Ce³⁺ and Ce⁴⁺ and releasing ROS (Mortezaee et al., 2019). SEM images of *S. aureus* and *E. coli* on the hydrogel surfaces of each group identify the additional pertinent bactericidal mechanisms, such as cell wall breakage and leakage of cell contents.

3.8 Anti-inflammatory activity of the PEA@CeO₂-QDs hydrogel

Numerous factors affect the phenotype of macrophages, which, in turn, alters the function exactly, known as coexisting traditionally activated (M1) and alternatively activated (M2) macrophages (Yunna et al., 2020). While M2 macrophages express arginase-1 (Arg-1), interleukin-10 (IL-10), and transforming growth factor-β (TGF-β) that are involved in angiogenesis, tissue healing, and anti-inflammatory processes, M1 macrophages principally express interleukin-1β (IL-1β), interleukin-6 (IL-6), and tumor necrosis factor-α (TNF-α) to prompt an inflammatory response (Locati et al., 2020; Xia et al., 2022). As a consequence, reducing the inflammatory milieu by controlling macrophage polarization is a successful strategy for treating inflammation.

A commonly used method to mimic bacterial infection and monitor inflammatory response is to employ LPS to polarize macrophages. The positive control group activated by LPS has significantly higher levels of IL-1β, IL-6, and TNF-α mRNA expression than the negative control group (Figures 7A–C), while IL-10, TGF-β, and Arg-1 mRNA expression is significantly lower (Figures 7D–F). Of note, the mRNA expression of IL-1β, IL-6, and TNF-α is significantly reduced in the leaching liquor of PEA and PEA@CeO₂-QDs hydrogels, while IL-10, TGF-β, and Arg-1 are significantly increased. The inhibitory effects on IL-1β and TNF-α mRNA expression with PEA@50CeO₂-QDs and PEA@75CeO₂-QDs hydrogels are detectable, but the enhancement with increasing concentration cannot be observed. However, for IL-6, the PEA@50CeO₂-QDs hydrogel shows the best inhibitory effect. Indeed, Arg-1 mRNA expression differs significantly between the PEA@50CeO₂-QDs and PEA@75CeO₂-QDs hydrogels, but the PEA@50CeO₂-QDs hydrogel group shows a much stronger effect of promoting expression. Overall, the PEA@50CeO₂-QDs hydrogel has a superior potential to induce M2 macrophage polarization.



Unexpectedly, the pure PEA hydrogel significantly boosts the expression of TGF- β mRNA while suppressing the expression of M1-type inflammatory cytokines (Figures 7A–C,E). In animal studies, Peng et al. (2021b) noted that the PEA hydrogel had a positive impact on the perforated site of the gastric mucosa. The pathological examination of tissue samples taken from the defect site reveals that the level of neutrophil and lymphocyte infiltration in the PEA group was significantly lower than that of the suture group and the fibrin group. Lin and Peng et al. discovered that the quantity of granulation and capillary formation in the defect was much higher than that in the blank control at the same time point, regardless of whether the PEA hydrogel was applied to the skin or mucosa (Peng et al., 2021b;

Lin et al., 2022). Therefore, the PEA hydrogel has a positive effect on inhibiting inflammation and promoting tissue healing.

One of the main pathophysiologicals of bacterial infection-related inflammation and aseptic inflammatory tissue damage is oxidative stress (Sies, 2015; Passi et al., 2020; Deng et al., 2021). Furthermore, CeO₂-QDs have outstanding antioxidant properties (Figures 5A–C). Ce exists more as Ce⁴⁺ in CeO₂-QDs. When the local inflammation is excessive, Ce⁴⁺ in CeO₂-QDs is converted to Ce³⁺, and the excessive ROS is removed to alleviate local inflammation. CeO₂ with a diameter of approximately 50 nm and a concentration of 25 μ g/mL was shown to cause 40% ROS scavenging in LPS-pretreated macrophages by Xia et al. (2008). CeO₂ with a

TABLE 1 Primer sequences used in this study.

Gene	Forward sequence	Reverse sequence
β -Actin	CATCCGTAAAGACCTCTAGCCAAC	ATGGAGCCACCAGATCCACA
IL-1 β	TCCAGGATGAGGACATGAGCAC	GAACGTCACACACCAGCAGGTTA
IL-6	CCACTTCACAAGTCGGAGGCTTA	CCAGTTTGGTAGCATCCATCATTTTC
TNF- α	ACTCCAGGCGGTGCCTATGT	GTGAGGGTCTGGGCCATAGAA
IL-10	ATGCTGCCTGCTCTTACTGACTG	CCCAAGTAACCCTTAAAGTCTCTGC
TGF- β	CTTCAGCCTCCACAGAGAAGAACT	TGTGTCCAGGCTCCAAATATAG
Arg-1	TCATGGAAGTGAACCCAACTCTTG	TCAGTCCCTGGCTTATGGTTACC

diameter of 5 nm, on the other hand, removed 100% of ROS in LPS-pretreated macrophages at a concentration of 1.4 $\mu\text{g}/\text{mL}$ (Wu and Ta, 2021). Rat *in vitro* tests exhibited decreased expression of pro-inflammatory factors like IL-1 β and COX-2, dominated by CeO₂ nanoparticles with particle diameters ranging from 4 to 20 nm, according to Oro et al. (2016). Muhammad et al. showed that LPS-stimulating RAW 264.7 cells treated with redox-active hollow CeO₂ nanospheres of smaller-diameter (4–10 nm) CeO₂ nanoparticles showed increased SOD- and CAT-like activities, together with the decreased expression of pro-inflammatory factors (Muhammad et al., 2022). We recognize that the reduction in CeO₂ nanoparticle or quantum size not only increases the enzyme mimic activity but also significantly enhances the anti-inflammatory effect. Accordingly, PEA@CeO₂-QDs, especially PEA@50CeO₂-QDs loading small-sized CeO₂ QDs, could exert an intensified anti-inflammatory effect.

4 Conclusion

We synthesized antibacterial and anti-inflammatory PEA@CeO₂-QDs materials. Combined with the preferable adhesion properties, the PEA hydrogel could serve as an appropriate substrate for CeO₂-QDs to play an enduring role in the wet tissue wound dressing. Due to their relatively slow rate of degradation, CeO₂-QDs have the potential to work for an extended period. Although the tensile, adhesion, and rheological properties of the hydrogel were decreased with the increase in the CeO₂-QDs doping amount (PEA@50CeO₂-QDs hydrogel and PEA@75CeO₂-QDs hydrogel), based on its self-healing abilities, the hydrogel structure could swiftly self-heal and regain structural integrity even if it gets disrupted. Additionally, PEA@CeO₂-QDs hydrogels were bio-secured and had stronger antioxidant activity and enzyme simulation activity with the increase in the doping dose.

Due to oxygen vacancies and size effects, the CeO₂-QDs had more Ce³⁺ than larger CeO₂ nanoparticles, resulting in stronger antibacterial properties. Among them, PEA@50CeO₂-QDs and PEA@75CeO₂-QDs hydrogels have better bactericidal effects. Meanwhile, the PEA@50CeO₂-QDs hydrogel has better anti-inflammatory effects and could induce macrophage M2-type polarization more potentially. Therefore, considering the

mechanical properties and bactericidal and anti-inflammatory effects of the material, the PEA@50CeO₂-QDs hydrogel may be valuable for the treatment of wet tissue wounds, as shown in Table 1.

Data availability statement

The original contributions presented in the study are included in the article/Supplementary Material; further inquiries can be directed to the corresponding authors.

Author contributions

WH: conceptualization, data curation, investigation, writing—original draft, and writing—review and editing. ZL: investigation, resources, and writing—original draft. XX: methodology, software, and writing—original draft. SS: formal analysis, resources, and writing—original draft. ZN: writing—original draft. JeL: supervision and writing—review and editing. JiL: formal analysis, resources, and writing—original draft. DY: visualization and writing—original draft. XL: conceptualization, funding acquisition, project administration, supervision, writing—original draft, and writing—review and editing.

Funding

The author(s) declare that financial support was received for the research, authorship, and/or publication of this article. The work was supported by the China Postdoctoral Science Foundation (2023M732676), the National Natural Science Foundation of China (2207206), the Open Funds of the State Key Laboratory of Rare Earth Resource Utilization (RERU2022022), the Open Research Fund of the Key Laboratory of the Ministry of Education for Advanced Catalysis Materials and Zhejiang Key Laboratory for Reactive Chemistry on Solid Surfaces, Zhejiang Normal University (KLMEACM202203), the Shandong Provincial Natural Science Foundation Youth Project (ZR2021QH251), and Clinical Medicine + X Research Project of the Affiliated Hospital of Qingdao University (QDFY + X2021055).

Conflict of interest

The authors declare that the research was conducted in the absence of any commercial or financial relationships that could be construed as a potential conflict of interest.

Publisher's note

All claims expressed in this article are solely those of the authors and do not necessarily represent those of their affiliated

organizations, or those of the publisher, the editors, and the reviewers. Any product that may be evaluated in this article, or claim that may be made by its manufacturer, is not guaranteed or endorsed by the publisher.

Supplementary material

The Supplementary Material for this article can be found online at: <https://www.frontiersin.org/articles/10.3389/fmats.2024.1379836/full#supplementary-material>

References

- Arumugam, A., Karthikeyan, C., Haja Hameed, A. S., Gopinath, K., Gowri, S., and Karthika, V. (2015). Synthesis of cerium oxide nanoparticles using *Gloriosa superba* L. leaf extract and their structural, optical and antibacterial properties. *Mater. Sci. Eng. C* 49, 408–415. doi:10.1016/j.msec.2015.01.042
- Babu, K. S., Anandkumar, M., Tsai, T. Y., Kao, T. H., Inbaraj, B. S., and Chen, B. H. (2020). Cytotoxicity and antibacterial activity of gold-supported cerium oxide nanoparticles. *Int. J. Nanomedicine* 9, 5515–5531. doi:10.2147/ijn.s70087
- Belusic-Gobic, M., Zubovic, A., Predrijevac, A., Harmicar, D., Cerovic, R., Udovic Gobic, S., et al. (2020). Microbiology of wound infection after oral cancer surgery. *J. Craniomaxillofac Surg.* 48 (7), 700–705. doi:10.1016/j.jcms.2020.05.011
- Bezkravnyi, O., Vorokhta, M., Pawlyta, M., Ptak, M., Piliat, L., Xie, X., et al. (2022). *In situ* observation of highly oxidized Ru species in Ru/CeO₂ catalyst under propane oxidation. *J. Mater. Chem. A* 10 (31), 16675–16684. doi:10.1039/d2ta02330j
- Brugnoli, L., Ferrari, A. M., Civalleri, B., Pedone, A., and Menziani, M. C. (2018). Assessment of density functional approximations for highly correlated oxides: the case of CeO₂ and Ce₂O₃. *J. Chem. Theory Comput.* 14 (9), 4914–4927. doi:10.1021/acs.jctc.8b00600
- Cao, H., Duan, L., Zhang, Y., Cao, J., and Zhang, K. (2021). Current hydrogel advances in physicochemical and biological response-driven biomedical application diversity. *Signal Transduct. Target. Ther.* 6 (1), 426. doi:10.1038/s41392-021-00830-x
- Carey, S. P., Rahman, A., Kraning-Rush, C. M., Romero, B., Somasegar, S., Torre, O. M., et al. (2015). Comparative mechanisms of cancer cell migration through 3D matrix and physiological microtracks. *Am. J. Physiology-Cell Physiology* 308 (6), C436–C447. doi:10.1152/ajpcell.00225.2014
- Chakrabarty, N., Dey, A., Krishnamurthy, S., and Chakraborty, A. K. (2021). CeO₂/Ce₂O₃ quantum dot decorated reduced graphene oxide nanohybrid as electrode for supercapacitor. *Appl. Surf. Sci.* 536, 147960. doi:10.1016/j.apsusc.2020.147960
- Chen, B. H., and Stephen Inbaraj, B. (2018). Various physicochemical and surface properties controlling the bioactivity of cerium oxide nanoparticles. *Crit. Rev. Biotechnol.* 38 (7), 1003–1024. doi:10.1080/07388551.2018.1426555
- Deng, L., Du, C., Song, P., Chen, T., Rui, S., Armstrong, D. G., et al. (2021). The role of oxidative stress and antioxidants in diabetic wound healing. *Oxid. Med. Cell Longev.* 2021, 1–11. doi:10.1155/2021/8852759
- Feehan, K. T., and Gilroy, D. W. (2019). Is resolution the end of inflammation? *Trends Mol. Med.* 25 (3), 198–214. doi:10.1016/j.molmed.2019.01.006
- Fu, J. Y., Lai, Y. X., Zheng, S. S., Wang, J., Wang, Y. X., Ren, K. F., et al. (2022). Mir-22-incorporated polyelectrolyte coating prevents intima hyperplasia after balloon-induced vascular injury. *Biomater. Sci.* 10 (13), 3612–3623. doi:10.1039/d2bm00536k
- Geng, L., Song, J., Zhou, Y., Xie, Y., Huang, J., Zhang, W., et al. (2016). CeO₂ nanorods anchored on mesoporous carbon as an efficient catalyst for imine synthesis. *Chem. Commun.* 52 (92), 13495–13498. doi:10.1039/c6cc05496j
- Greish, K. (2010). Enhanced permeability and retention (EPR) effect for anticancer nanomedicine drug targeting. *Methods Mol. Biol. Clift. NJ* 624, 25–37. doi:10.1007/978-1-60761-609-2_3
- Grinter, D. C., Allan, M., Yang, H. J., Salcedo, A., Murgida, G. E., Shaw, B. J., et al. (2021). Ce=O terminated CeO₂. *Angew. Chem. Int. Ed.* 60 (25), 13835–13839. doi:10.1002/anie.202101771
- Guan, T., Li, J., Chen, C., and Liu, Y. (2022). Self-assembling peptide-based hydrogels for wound tissue repair. *Adv. Sci. (Weinh)* 9 (10), e2104165. doi:10.1002/advs.202104165
- Hosseini, M., and Mozafari, M. (2020). Cerium oxide nanoparticles: recent advances in tissue engineering. *Mater. (Basel)* 13 (14), 3072. doi:10.3390/ma13143072
- Hu, P., An, J., Faulkner, M. M., Wu, H., Li, Z., Tian, X., et al. (2020). Nanoparticle charge and size control foliar delivery efficiency to plant cells and organelles. *ACS Nano* 14 (7), 7970–7986. doi:10.1021/acsnano.9b09178
- Ikram, M., Hayat, S., Imran, M., Haider, A., Naz, S., Ul-Hamid, A., et al. (2021). Novel Ag/cellulose-doped CeO₂ quantum dots for efficient dye degradation and bactericidal activity with molecular docking study. *Carbohydr. Polym.* 269, 118346. doi:10.1016/j.carbpol.2021.118346
- Ji, C. H., Lee, S. J., and Oh, S. Y. (2019). P3HT-based visible-light organic photodetectors using PEI/PAA multilayers as a p-type buffer layer. *RSC Adv.* 9 (64), 37180–37187. doi:10.1039/c9ra08568h
- Jia, Z. G., Li, W., and Zhou, Z. R. (2015). Mechanical characterization of stomach tissue under uniaxial tensile action. *J. Biomech.* 48 (4), 651–658. doi:10.1016/j.jbiomech.2014.12.048
- Ju, X., Hubalek Kalbacova, M., Šmíd, B., Johánek, V., Janata, M., Dinová, T. N., et al. (2021). Poly(acrylic acid)-mediated synthesis of cerium oxide nanoparticles with variable oxidation states and their effect on regulating the intracellular ROS level. *J. Mater. Chem. B* 9 (36), 7386–7400. doi:10.1039/d1tb00706h
- Kannan, S. K., and Sundrarajan, M. (2014). A green approach for the synthesis of a cerium oxide nanoparticle: characterization and antibacterial activity. *Int. J. Nanosci.* 13 (03), 1450018. doi:10.1142/s0219581x14500185
- Kar, T., Casales-Díaz, M., Ramos-Hernández, J. J., Sotelo-Mazón, O., Henao, J., Valdez Rodríguez, S., et al. (2022). CeO₂-x quantum dots decorated nitrogen-doped hollow porous carbon for supercapacitors. *J. Colloid Interface Sci.* 622, 147–155. doi:10.1016/j.jcis.2022.04.114
- Kilic, M. E., Lee, J.-H., and Lee, K.-R. (2021). Oxygen ion transport in doped ceria: effect of vacancy trapping. *J. Mater. Chem. A* 9 (24), 13883–13889. doi:10.1039/d1ta00926e
- Kim, Y. G., Lee, Y., Lee, N., Soh, M., Kim, D., and Hyeon, T. (2023). Ceria-based therapeutic antioxidants for biomedical applications. *Adv. Mat.* 36, e2210819. doi:10.1002/adma.202210819
- Kitamoto, S., Nagao-Kitamoto, H., Hein, R., Schmidt, T. M., and Kamada, N. (2020). The bacterial connection between the oral cavity and the gut diseases. *J. Dent. Res.* 99 (9), 1021–1029. doi:10.1177/0022034520924633
- Kolaczowska, E., and Kubek, P. (2013). Neutrophil recruitment and function in health and inflammation. *Nat. Rev. Immunol.* 13 (3), 159–175. doi:10.1038/nri3399
- Kong, Q., Cui, K., Zhang, L., Wang, Y., Sun, J., Ge, S., et al. (2018). “On-Off-On” photoelectrochemical/visual lab-on-paper sensing via signal amplification of CdS quantum Dots@Leaf-shape ZnO and quenching of Au-modified prism-anchored octahedral CeO₂ nanoparticles. *Anal. Chem.* 90 (19), 11297–11304. doi:10.1021/acs.analchem.8b01844
- Kumar, K. M., Mahendhiran, M., Diaz, M. C., Hernandez-Como, N., Hernandez-Eligio, A., Torres-Torres, G., et al. (2018). Green synthesis of Ce³⁺ rich CeO₂ nanoparticles and its antimicrobial studies. *Mater. Lett.* 214, 15–19. doi:10.1016/j.matlet.2017.11.097
- Li, J., van Ewijk, G., van Dijken, D. J., van der Gucht, J., and de Vos, W. M. (2021). Single-step application of polyelectrolyte complex films as oxygen barrier coatings. *ACS Appl. Mater. Interfaces* 13 (18), 21844–21853. doi:10.1021/acsmi.1c05031
- Li, R., Wen, C., Yan, K., Liu, T., Zhang, B., Xu, M., et al. (2023). The water splitting cycle for hydrogen production at photo-induced oxygen vacancies using solar energy: experiments and DFT calculation on pure and metal-doped CeO₂. *J. Mater. Chem. A* 11 (13), 7128–7141. doi:10.1039/d2ta08833a
- Liman, R., Acikbas, Y., and Cigerci, İ. H. (2019). Cytotoxicity and genotoxicity of cerium oxide micro and nanoparticles by Allium and Comet tests. *Ecotoxicol. Environ. Saf.* 168, 408–414. doi:10.1016/j.ecoenv.2018.10.088
- Lin, Z., Fan, D., Li, G., He, L., Qin, X., Zhao, B., et al. (2022). Antibacterial, adhesive, and conductive hydrogel for diabetic wound healing. *Macromol. Biosci.* 23 (2), e2200349. doi:10.1002/mabi.202200349

- Liu, Y., Li, H., Liu, W., Guo, J., Yang, H., Tang, H., et al. (2022). Design of monovalent cerium-based metal organic frameworks as bioinspired superoxide dismutase mimics for ionizing radiation protection. *ACS Appl. Mater. Interfaces* 14 (49), 54587–54597. doi:10.1021/acsmi.2c17358
- Locati, M., Curtale, G., and Mantovani, A. (2020). Diversity, mechanisms, and significance of macrophage plasticity. *Annu. Rev. Pathol.* 15, 123–147. doi:10.1146/annurev-pathmechdis-012418-012718
- Luneau, M., Strandberg, L., Montserrat-Sisó, G., Shokhen, V., Mohan, R., Grönbeck, H., et al. (2023). Fundamental insight into enhanced activity of Pd/CeO₂ thin films in hydrogen oxidation reaction in alkaline media. *J. Mater. Chem. A* 11 (30), 16370–16382. doi:10.1039/d3ta01879b
- Luo, D., Chen, B., Li, X., Liu, Z., Liu, X., Liu, X., et al. (2018). Three-dimensional nitrogen-doped porous carbon anchored CeO₂ quantum dots as an efficient catalyst for formaldehyde oxidation. *J. Mater. Chem. A* 6 (17), 7897–7902. doi:10.1039/c8ta00076j
- Mahapatra, C., Singh, R. K., Lee, J.-H., Jung, J., Hyun, J. K., and Kim, H.-W. (2017). Nano-shape varied cerium oxide nanomaterials rescue human dental stem cells from oxidative insult through intracellular or extracellular actions. *Acta Biomater.* 50, 142–153. doi:10.1016/j.actbio.2016.12.014
- McColl, D., Cartlidge, B., and Connolly, P. (2007). Real-time monitoring of moisture levels in wound dressings *in vitro*: an experimental study. *Int. J. Surg.* 5 (5), 316–322. doi:10.1016/j.ijsu.2007.02.008
- Meng, W., Sun, S., Xie, D., Dai, S., Shao, W., Zhang, Q., et al. (2024). Engineering defective Co₃O₄ containing both metal doping and vacancy in octahedral cobalt site as high performance catalyst for methane oxidation. *Mol. Catal.* 553, 113768. doi:10.1016/j.mcat.2023.113768
- Monika, P., Chandrababha, M. N., Rangarajan, A., Waiker, P. V., and Chidambaramurthy, K. N. (2021). Challenges in healing wound: role of complementary and alternative medicine. *Front. Nutr.* 8, 791899. doi:10.3389/fnut.2021.791899
- Mortezaee, K., Najafi, M., Samadian, H., Barabadi, H., Azarnezhad, A., and Ahmadi, A. (2019). Redox interactions and genotoxicity of metal-based nanoparticles: a comprehensive review. *Chemico-Biological Interact.* 312, 108814. doi:10.1016/j.cbi.2019.108814
- Muhammad, F., Huang, F., Cheng, Y., Chen, X., Wang, Q., Zhu, C., et al. (2022). Nanoceria as an electron reservoir: spontaneous deposition of metal nanoparticles on oxides and their anti-inflammatory activities. *ACS Nano* 16 (12), 20567–20576. doi:10.1021/acsnano.2c07306
- Nadeem, M., Khan, R., Afridi, K., Nadhman, A., Ullah, S., Faisal, S., et al. (2020). <p>Green Synthesis of Cerium Oxide Nanoparticles (CeO₂ NPs) and Their Antimicrobial Applications: a Review</p>. *Int. J. Nanomedicine* 15, 5951–5961. doi:10.2147/ijn.s255784
- Naidi, S. N., Harunsani, M. H., Tan, A. L., and Khan, M. M. (2021a). Green-synthesized CeO₂ nanoparticles for photocatalytic, antimicrobial, antioxidant and cytotoxicity activities. *J. Mater. Chem. B* 9 (28), 5599–5620. doi:10.1039/d1tb00248a
- Naidi, S. N., Khan, F., Tan, A. L., Harunsani, M. H., Kim, Y.-M., and Khan, M. M. (2021b). Green synthesis of CeO₂ and Zr/Sn-dual doped CeO₂ nanoparticles with photoantioxidant and antibiofilm activities. *Biomaterials Sci.* 9 (14), 4854–4869. doi:10.1039/d1bm00298h
- Nelson, B., Johnson, M., Walker, M., Riley, K., and Sims, C. (2016). Antioxidant cerium oxide nanoparticles in biology and medicine. *Antioxidants* 5 (2), 15. doi:10.3390/antiox5020015
- Oro, D., Yudina, T., Fernandez-Varo, G., Casals, E., Reichenbach, V., Casals, G., et al. (2016). Cerium oxide nanoparticles reduce steatosis, portal hypertension and display anti-inflammatory properties in rats with liver fibrosis. *J. Hepatol.* 64 (3), 691–698. doi:10.1016/j.jhep.2015.10.020
- Passi, M., Kumar, V., and Packirisamy, G. (2020). Theranostic nanozyme: silk fibroin based multifunctional nanocomposites to combat oxidative stress. *Mater. Sci. Eng. C Mater. Biol. Appl.* 107, 110255. doi:10.1016/j.msec.2019.110255
- Peng, X., Xia, X., Xu, X., Yang, X., Yang, B., Zhao, P., et al. (2021b). Ultrafast self-gelling powder mediates robust wet adhesion to promote healing of gastrointestinal perforations. *Sci. Adv.* 7 (23), eabe8739. doi:10.1126/sciadv.abe8739
- Peng, X., Xu, X., Deng, Y., Xie, X., Xu, L., Xu, X., et al. (2021a). Ultrafast self-gelling and wet adhesive powder for acute hemostasis and wound healing. *Adv. Funct. Mater.* 31 (33), doi:10.1002/adfm.202102583
- Pisal, V., Wakchaure, P., Patil, N., and Bhagwat, S. (2019). Green synthesized CeO₂ quantum dots: a study of its antimicrobial potential. *Mater. Res. Express* 6 (11), 115409. doi:10.1088/2053-1591/ab4fa5
- Ren, S., Zhou, Y., Zheng, K., Xu, X., Yang, J., Wang, X., et al. (2022). Cerium oxide nanoparticles loaded nanofibrous membranes promote bone regeneration for periodontal tissue engineering. *Bioact. Mater.* 7, 242–253. doi:10.1016/j.bioactmat.2021.05.037
- Schaube, M., Merkle, R., and Maier, J. (2019). Oxygen exchange kinetics on systematically doped ceria: a pulsed isotope exchange study. *J. Mater. Chem. A* 7 (38), 21854–21866. doi:10.1039/c9ta05908c
- Shahzadi, A., Moeen, S., Khan, A. D., Haider, A., Haider, J., Ul-Hamid, A., et al. (2023). La-doped CeO₂ quantum dots: novel dye degrader, antibacterial activity, and *in silico* molecular docking analysis. *ACS Omega* 8 (9), 8605–8616. doi:10.1021/acsomega.2c07753
- Sies, H. (2015). Oxidative stress: a concept in redox biology and medicine. *Redox Biol.* 4, 180–183. doi:10.1016/j.redox.2015.01.002
- Singh, S., Dosani, T., Karakoti, A. S., Kumar, A., Seal, S., and Self, W. T. (2011). A phosphate-dependent shift in redox state of cerium oxide nanoparticles and its effects on catalytic properties. *Biomaterials* 32 (28), 6745–6753. doi:10.1016/j.biomaterials.2011.05.073
- Sukhanova, A., Bozrova, S., Gerasimovich, E., Baryshnikova, M., Sokolova, Z., Samokhvalov, P., et al. (2022). Dependence of quantum dot toxicity *in vitro* on their size, chemical composition, and surface charge. *Nanomaterials* 12 (16), 2734. doi:10.3390/nano12162734
- Taubenberger, A. V., Girardo, S., Träber, N., Fischer-Friedrich, E., Kräter, M., Wagner, K., et al. (2019). 3D microenvironment stiffness regulates tumor spheroid growth and mechanics via p21 and ROCK. *Adv. Biosyst.* 3 (9), e1900128. doi:10.1002/adbi.201900128
- Van Lehn, R. C., Atukorale, P. U., Carney, R. P., Yang, Y.-S., Stellacci, F., Irvine, D. J., et al. (2013). Effect of particle diameter and surface composition on the spontaneous fusion of monolayer-protected gold nanoparticles with lipid bilayers. *Nano Lett.* 13 (9), 4060–4067. doi:10.1021/nl401365n
- Wang, H., Liu, Y., Cai, K., Zhang, B., Tang, S., Zhang, W., et al. (2021b). Antibacterial polysaccharide-based hydrogel dressing containing plant essential oil for burn wound healing. *Burns Trauma* 9, tkab041. doi:10.1093/burnst/tkab041
- Wang, S., Wu, C.-T., Wang, J., Zhang, C., Fan, Z., Wang, H., et al. (2019). Maintained properties of aged dental pulp stem cells for superior periodontal tissue regeneration. *Aging Dis.* 10 (4), 793. doi:10.14336/ad.2018.0729
- Wang, X., Fang, X., Gao, X., Wang, H., Li, S., Li, C., et al. (2022). Strong adhesive and drug-loaded hydrogels for enhancing bone-implant interface fixation and anti-infection properties. *Colloids Surf. B Biointerfaces* 219, 112817. doi:10.1016/j.colsurfb.2022.112817
- Wang, Y., Li, C., Wan, Y., Qi, M., Chen, Q., Sun, Y., et al. (2021a). Quercetin-loaded ceria nanocomposite potentiate dual-directional immunoregulation via macrophage polarization against periodontal inflammation. *Small* 17 (41), e2101505. doi:10.1002/sml.202101505
- Wu, Y., and Ta, H. T. (2021). Different approaches to synthesising cerium oxide nanoparticles and their corresponding physical characteristics, and ROS scavenging and anti-inflammatory capabilities. *J. Mater. Chem. B* 9 (36), 7291–7301. doi:10.1039/d1tb01091c
- Xia, P., Cao, S., Zhu, B., Liu, M., Shi, M., Yu, J., et al. (2020). Designing a 0D/2D S-scheme heterojunction over polymeric carbon nitride for visible-light photocatalytic inactivation of bacteria. *Angew. Chem. Int. Ed.* 59 (13), 5218–5225. doi:10.1002/anie.201916012
- Xia, T., Kovochich, M., Liang, M., Madler, M., Gilbert, B., Shi, H., et al. (2008). Comparison of the mechanism of toxicity of zinc oxide and cerium oxide nanoparticles based on dissolution and oxidative stress properties. *ACS Nano* 2 (10), 2121–2134. doi:10.1021/nm800511k
- Xia, X., Song, X., Li, Y., Hou, W., Lv, H., Li, F., et al. (2022). Antibacterial and anti-inflammatory ZIF-8@Rutin nanocomposite as an efficient agent for accelerating infected wound healing. *Front. Bioeng. Biotechnol.* 10, 1026743. doi:10.3389/fbioe.2022.1026743
- Xue, Y., Luan, Q., Yang, D., Yao, X., and Zhou, K. (2011). Direct evidence for hydroxyl radical scavenging activity of cerium oxide nanoparticles. *J. Phys. Chem. C* 115 (11), 4433–4438. doi:10.1021/jp109819u
- Yadav, N., Patel, V., McCourt, L., Ruppert, M., Miller, M., Inerbaev, T., et al. (2022). Tuning the enzyme-like activities of cerium oxide nanoparticles using a triethyl phosphite ligand. *Biomater. Sci.* 10 (12), 3245–3258. doi:10.1039/d2bm00396a
- Yadav, N., and Singh, S. (2021). Polyoxometalate-Mediated vacancy-engineered cerium oxide nanoparticles exhibiting controlled biological enzyme-mimicking activities. *Inorg. Chem.* 60 (10), 7475–7489. doi:10.1021/acs.inorgchem.1c00766
- Yang, B., Chen, Y., and Shi, J. (2019). Reactive oxygen species (ROS)-Based nanomedicine. *Chem. Rev.* 119 (8), 4881–4985. doi:10.1021/acs.chemrev.8b00626
- Yang, J., Yang, Z., Li, J., Gang, H., Mei, D., Yin, D., et al. (2024). Engineering a hollow bowl-like porous carbon-confined Ru-MgO hetero-structured nanopair as a high-performance catalyst for ammonia borane hydrolysis. *Mater. Horiz.* 2024, 1909. doi:10.1039/d3mh01909h
- Younis, A., Chu, D., Lin, X., Yi, J., Dang, F., and Li, S. (2013). High-performance nanocomposite based memristor with controlled quantum dots as charge traps. *ACS Appl. Mater. Interfaces* 5 (6), 2249–2254. doi:10.1021/am400168m
- Yunna, C., Mengru, H., Lei, W., and Weidong, C. (2020). Macrophage M1/M2 polarization. *Eur. J. Pharmacol.* 877, 173090. doi:10.1016/j.ejphar.2020.173090
- Zhuo, M., Ma, J., and Quan, X. (2021). Cytotoxicity of functionalized CeO₂ nanoparticles towards *Escherichia coli* and adaptive response of membrane properties. *Chemosphere* 281, 130865. doi:10.1016/j.chemosphere.2021.130865